Longitudinal *in vivo* micro-CT-based approach allows spatio-temporal characterization of fracture healing patterns and assessment of biomaterials in mouse femur defect models

Esther Wehrle[1], Duncan C Tourolle né Betts[1], Gisela A Kuhn[1], Erica Floreani[1], Malavika H Nambiar[1], Bryant J Schroeder[1], Sandra Hofmann[1,2], Ralph Müller[1]

[1] Institute for Biomechanics, ETH Zurich, Zurich, Switzerland, [2] Department of Biomedical Engineering and Institute for Complex Molecular Systems, Eindhoven University of Technology, The Netherlands.

Corresponding author:

Ralph Müller, PhD

Institute for Biomechanics

ETH Zurich

Leopold-Ruzicka-Weg 4

8093 Zurich, Switzerland

Email: ram@ethz.ch

Abstract

Thorough preclinical evaluation of novel biomaterials for treatment of large bone defects is essential prior to clinical application. Using *in vivo* micro-computed tomography (micro-CT) and mouse femoral defect models with different defect sizes, we were able to detect spatio-temporal healing patterns indicative of physiological and impaired healing in three defect sub-volumes and the adjacent cortex. The time-lapsed *in vivo* micro-CT-based approach was then applied to evaluate the bone regeneration potential of biomaterials using collagen and BMP-2 as test materials. Both collagen and BMP-2 treatment led to distinct changes in bone turnover in the different healing phases. Despite increased periosteal bone formation, 87.5% of the defects treated with collagen scaffolds resulted in non-unions. Additional BMP-2 application significantly accelerated the healing process and increased the union rate to 100%. This study further shows potential of time-lapsed *in vivo* micro-CT for capturing spatio-temporal deviations preceding non-union formation and how this can be prevented by application of biomaterials.

This study therefore supports the application of longitudinal *in vivo* micro-CT for discrimination of normal and disturbed healing patterns and for the spatio-temporal characterization of the bone regeneration capacity of biomaterials.

Introduction

Regeneration and healing of large bone defects (e.g. caused by trauma, infection, tumor resection, congenital skeletal disorders) is a treatment challenge in orthopedic surgery with as much as 10-20% of patients experiencing delayed or non-unions [1-3]. Recent advances in tissue engineering and material sciences (e.g. 3D-bioprinting) enabled the development of diverse biomaterials, which can be functionalized with biochemical factors (e.g. growth factors) and combined with cell therapeutic approaches [3-5]. In order to facilitate the clinical application of these innovative approaches for the treatment of large bone defects, their bone regeneration capacity needs to be systematically and thoroughly characterized in preclinical studies [6-8]. For this purpose, critical size defect models have been developed for load-bearing and non-load-bearing bones in small and large animals [7,9-13]. So far, most of these studies focused their evaluation on end-point radiological and histological analysis [14-16]. However, recent studies indicate that longitudinal non-invasive imaging could improve the evaluation of a biomaterial's bone regeneration capacity, due to the ability to follow the regeneration process in the same animal over time, thereby also reducing animal numbers according to the 3R's of animal welfare [17,18]. Particularly, *in vivo* micro-CT was shown to be suitable for the assessment of bone tissue formation and mineralization after biomaterial application in critical size defect models [17-19]. A further development is the consecutive registration of time-lapsed *in vivo* images [20]. We recently developed a longitudinal *in vivo* micro-CT-based approach for healing-phase-specific monitoring of fracture repair in mouse femur defect models [21]. Registration of consecutive scans using a branching scheme (bridged vs. unbridged defect) combined with a two/multi-threshold approach enabled the assessment of localized bone turnover and mineralization kinetics relevant for monitoring

60 callus remodelling [21,22]. Furthermore, we showed that longitudinal *in vivo* micro-CT imaging
61 itself did not significantly affect callus formation and remodelling [22].

62 It is well accepted that longitudinal non-invasive imaging of the healing process is
63 advantageous compared to cross-sectional study designs[22]. In order to apply *in vivo* micro-
64 CT-based longitudinal monitoring approaches for the evaluation of biomaterials, it has to be
65 assessed, whether these approaches allow for reliable discrimination between normal and
66 impaired healing conditions (e.g. critical-sized defects). So far, preclinical studies were often
67 not able to reliably capture the bone healing potential of biomaterials due to limitations in
68 study design: (I) cross-sectional setup, (II) assessment not considering defect sub-volumes,
69 (III) assessment not specific to the healing phases.

70 Therefore, this study assesses whether our recently developed time-lapsed micro-CT based
71 monitoring approach is suitable for discrimination of healing patterns associated with
72 physiological and impaired bone healing conditions using mouse femur defect models with
73 different gap sizes. In a second step, we evaluated whether the time-lapsed *in vivo* micro-CT-
74 based monitoring approach is suitable for profound characterization of the bone
75 regeneration capacity of biomaterials using well characterized porous collagen scaffolds and
76 bone morphogenetic protein (BMP-2) as example materials.

77

78 **Results**

79 In Experiment 1, we assessed the potential of time-lapsed *in vivo* micro-CT for reliable
80 discrimination between physiological and impaired fracture healing patterns. We compared
81 the healing process (week 0-6) in mice receiving either a small (0.9mm, n=10) or large femur

82 defect (2mm, n=8; Fig. 1; Supplementary Video 1). Via registration of consecutive micro-CT
83 scans, structural and dynamic callus parameters were followed in three callus sub-volumes
84 (defect center, DC; defect periphery, DP; cortical fragment periphery, FP) and the adjacent
85 cortical fragments (FC) over time (Fig. 1, 2). In Experiment 2, we applied the same time-
86 lapsed *in vivo* imaging approach to assess the bone regeneration capacity of collagen
87 scaffolds (n=8) and collagen scaffolds+BMP-2 (n=8; Fig. 3, 4, Supplementary Video 2; for
88 detailed study design see Supplementary Table S1).

89 **General physical observation**

90 Post-operative monitoring was performed with a scoring system defined in licence number
91 36/2014 (Kantonales Veterinäramt Zürich, Zurich, Switzerland), evaluating the following
92 parameters: social behaviour, body position, motion, load bearing of operated limb, habitus,
93 surgery wound. Scoring values: 0-4 (0=normal, 4=severely impaired, end-point criteria:
94 scored 4 in one category or overall score ≥8). Monitoring schedule: evening of surgery day,
95 day 1-3: morning and evening, day 4 until end of experiment: 3x/week, daily if scored ≥2 in
96 one criterion. All mice recovered rapidly from surgery. However, one animal from the 0.9mm
97 defect group only showed minor load bearing of the operated limb in the first post-operative
98 week, which then gradually increased, reaching normal values after 2 weeks. The body
99 weight did not significantly change during the healing period and did not differ between the
100 groups in Experiment 1 and 2 (see Supplementary Fig. 1 and 2). Social interaction between
101 mice and nesting behaviour did not differ from pre-surgical observations and were similar
102 for animals from all groups.

103

104 **VOIs for evaluation by time-lapsed *in vivo* micro-CT**

105 **Experiment 1:**

106 In order to exclude bias in the further micro-CT analyses, we compared the size of the two
107 central VOIs (DC, FC) used for normalization of CT parameters (depicted in Fig. 2) between
108 groups. One animal from the 2.0mm group could not be included in the analysis due to
109 incorrect registration caused by differences in leg alignment between micro-CT scans. The
110 two central VOIs encompassed the following volume for the 0.9mm group (n=10) and the
111 2.0mm group (n=7) with significant group differences given in brackets: 1.64±0.19mm^3 vs.
112 3.45±0.18mm^3 for DC ($p<0.0001$), and 3.18±0.12mm^3 vs. 0.94±0.30mm^3 for FC ($p<0.0001$).

113 **Experiment 2:**

114 The DC and FC VOIs encompassed the following volume for the collagen group (n=8) and the
115 collagen+BMP-2 group (n=8): 3.09±0.22mm^3 vs. 3.15±0.22mm^3 for DC and 1.25±0.26mm^3 vs.
116 1.47±0.19mm^3 for FC. No significant group differences in VOI size were detected between
117 the two groups.

118

119 **Longitudinal monitoring of fracture healing by time-lapsed *in vivo* micro-CT in non-critical**
120 **and critical-sized femur defects (Experiment 1)**

121 In both groups the repeated micro-CT scans (1x/week, Fig. 1, Supplementary Video 1)
122 covered the period from the day of the defect surgery (d0) until post-operative week 6. In
123 the 0.9mm group, distinct callus characteristics indicative of the different healing phases
124 (inflammation, repair, remodelling) were seen in the three callus VOIS (DC, DP, FP; Fig. 1 and
125 Fig. 2) as previously described in the same femur defect model [22]. Specifically, a strong
126 increase in bone formation with maximum values in week 1-2 (BFR: DC - 3.67±1.50%) and
127 week 2-3 (BFR: DP - 2.44 ±1.31%, FP - 2.50±0.89%; Fig. 2) indicated the progression from the

128 inflammation to the repair phase. This triggered bone resorption with maximum values seen
129 in week 2-3 (BRR: DC - 1.15±0.48%) and week 3-4 (BRR: DP - 0.82±0.74%, FP - 0.86±0.48%)
130 indicating progression to the remodelling phase. In all callus VOIs a significant up to 95x (DP)
131 increase ($p<0.0001$ for all VOIs) in bone volume was seen over time with maximum values
132 observed in week 4 (BV/TV: DC - 44±9%, DP - 24±10%, FP - 29±8%). From week 2 onwards,
133 the fraction of highly mineralized bone continuously increased in all callus VOIs until the
134 study endpoint (week 6).
135 In the 2.0mm defect group, only a slight onset in bone formation was seen in the callus VOIs
136 from week 0-1 to week 1-2 without characteristic peak values in the further healing process
137 (Fig. 1 and 2). We could also not observe any significant gain in bone volume throughout the
138 healing period, indicating an impaired and delayed healing pattern. Nevertheless, we saw a
139 continuous increase in the fraction of highly mineralized bone in all callus VOIs, indicating no
140 substantial disturbances of callus mineralization, despite the small callus volume.
141 Comparison of both groups (0.9mm defect, 2.0mm defect) showed similar patterns in
142 healing initiation with bone formation, first starting in the defect center (DC) and the cortical
143 fragment periphery (FP) from week 0-1 to week 1-2. However, in the DC VOI the increase in
144 bone formation (6x) was significantly lower ($p=0.001$) in the 2mm group compared to the
145 0.9mm group (19x) and the bone formation rates then remained stable at low values
146 (≤0.95%/day) throughout the healing period associated with only little endosteal callus
147 formation. In the FP VOI, the increase in bone formation from week 0-1 to week 1-2 was
148 similar for both groups, but the 2.0mm defect group then showed a sudden decline (-40%) in
149 bone formation (week 1-2 vs week 2-3) leading to premature cessation of periosteal callus
150 formation. In the defect periphery (DP) hardly any callus formation (BFR ≤0.21%/day) was

151 seen in the 2.0mm defect group throughout the healing period leading to significantly
152 smaller callus dimensions compared to the 0.9mm group from week 3 until the study end
153 (p=0.0001). With respect to bone resorption, no significant differences between the two
154 defect groups were seen in the early healing period (week 0-1, week 1-2) in any of the callus
155 sub-volumes. However, in the later healing period, bone resorption was significantly lower in
156 the 2.0mm defect group compared to the 0.9mm defect group in the DC (week 2-3: p=0.047,
157 week 4-5: p=0.0064), FP (week 2-3: p= 0.0045, week 5-6: p=0.0048) and DP (week 4-5:
158 p=0.0157, week 5-6: p=0.0177) VOIs, indicating impaired bone remodelling. By week 6, not
159 only the bone volume, but also the fraction of highly mineralized bone was lower in all callus
160 sub-volumes in the 2.0mm defect group compared to the 0.9mm defect group with
161 significant differences (p=0.0383) being observed in the DP sub-volume (BV_{645}/BV_{395}: 2.0mm
162 group - 63±11%, 0.9mm group - 82±4%).
163
164 To assess functional healing outcome, we particularly focused on the defect VOIs (DC+DP)
165 which are most important for evaluating later healing time points during the remodelling
166 phase of fracture healing. The previously observed differences in bone turnover, bone
167 volume and mineralization between the two groups also affected cortical bridging.
168 According to the standard clinical evaluation of X-rays, the number of bridged cortices per
169 callus was evaluated in two perpendicular planes and animals with ≥3 bridged cortices were
170 categorized as healed. Cortical bridging first occurred by week 3 in 70% of the animals in the
171 0.9mm defect group, whereas none of the animals in the 2.0mm group showed bridged
172 cortices at this time point (Table 1). By week 6, 90% of the 0.9mm defects were categorized

173 as healed with only 1 defect being classified as non-union. In contrast, in the 2.0mm defect
174 group only 1 animal showed cortical bridging and 87.5% manifested as non-unions.
175
176 Bone turnover in the cortical fragments (FC) showed a similar pattern in both groups,
177 without characteristic peak values in bone formation and resorption rates. Specifically,
178 maximum bone formation rates were significantly lower (0.9mm group: -80%, $p<0.0001$,
179 2.0mm group: -58%, $p=0.004$) compared to those observed in the periosteal region (FP).
180 Furthermore, a negative bone turnover was seen with maximum resorption rates (BRR in
181 week 2-3; 0.79±0.15%) exceeding bone formation rates (BFR in week 2-3: 0.49±0.37%) in the
182 0.9mm group. This resulted in a decrease in bone volume over time (0.9mm group: -19%,
183 2.0mm group: -57%). Additionally, a significant 8% (0.9mm group, $p=0.0017$) and 11%
184 (2.0mm group, $p=0.0072$) decrease in the fraction of highly mineralized bone was seen from
185 week 1 to week 3 suggesting reorganization of the cortical bone adjacent to the forming and
186 remodelling fracture callus.
187
188 **Longitudinal assessment of biomaterials by time-lapsed *in vivo* micro-CT in critical-sized**
189 **femur defects (Experiment 2)**
190 In the collagen group, no significant weekly changes in bone formation rate were seen in the
191 central defect VOIs (DC, DP; Fig. 3 and 4; Supplementary Video 2). Bone resorption rates
192 slightly but significantly increased during the early healing period (DC: 7.6x from week 0-1 to
193 week 1-2, DP: 4.3x from week 0-1 to week 1-2) and then decreased (DC) or remained stable
194 (DP) from week 2-3 to week 5-6. This led to only little callus formation in these central VOIs,
195 as similarly seen in the 2mm defect group from Experiment 1, indicating an impaired

196 endosteal fracture healing pattern associated with the application of the collagen scaffolds.
197 In the periosteal VOI (FP) a significant 3.2x increase in bone formation rate was seen from
198 week 0-1 to week 1-2, which remained stable during the subsequent week, before
199 decreasing after week 2-3 reaching baseline values by week 5-6. No significant changes were
200 seen in the bone resorption rate throughout the healing process. Compared to the 2mm
201 defect group from Experiment 1, similar periosteal callus volumes were observed in the early
202 healing period (BV/TV in week 2: collagen group: 13.08±4.88%, 2mm defect group:
203 15.99±5.09%). In the collagen group, the periosteal callus volume further increased (+53%)
204 from week 2 to week 3, whereas it decreased (-30%) in the 2mm defect group during the
205 same period, suggesting changes in periosteal callus formation potentially associated with
206 the application of the collagen scaffolds.
207 In the collagen+BMP-2 group a similar healing pattern compared to the collagen group was
208 seen in the defect center (DC). Nevertheless, BMP-2 application led to a significantly 2.1x
209 increased bone formation rate in week 1-2 compared to the collagen group, which was also
210 associated with a transiently increased mineralized callus volume in this endosteal VOI in
211 week 2. However, in week 6, both groups showed similar callus volumes and fraction of
212 highly mineralized bone, indicating only a slight and transient BMP-2 associated effect on
213 callus formation and remodelling in the defect center. In contrast, in DP and FP VOIs a
214 completely different picture was seen: Compared to the collagen group, a sudden 17x (DP)
215 and 3.6x (FP) induction in BFR already from week 0-1 to week 1-2 was detected. This
216 indicates that collagen+BMP-2 scaffolds are able to induce bone formation at defect
217 locations distant to the cortical bone potentially allowing healing of large defects. The BMP-2
218 induced increase in the bone formation rate was higher but persisted shorter compared to

219 the 0.9mm defect group with uncompromised healing in Experiment 1. This led to a
220 significant 318x (DP) and 9.1x (FP) increase in bone volume by week 2 (DP: $p<0.0001$; FP:
221 $p=0.0002$). The periosteal callus volume significantly ($p<0.0001$ for DP and FP) exceeded the
222 values of the collagen group and was also higher compared to the 0.9mm group from
223 Experiment 1. In both VOIs a significant 63x (DP) and 10x (FP) increase in bone resorption
224 was seen from week 1-2 to week 2-3 ($p<0.0001$ for both VOIs), indicating early onset of
225 callus remodelling. The bone resorption rates then remained at significantly higher levels
226 compared to the collagen group and both groups from Experiment 1, indicating pronounced
227 callus remodelling in the collagen+BMP-2 group. The fraction of highly mineralized tissue
228 remained significantly lower in the collagen+BMP-2 group indicating that the remodelling
229 process was still ongoing, whereas the bone healing process had finished in all other groups.
230 Despite the BMP-2 associated improved healing outcome, the healing pattern was
231 completely different compared to the 0.9mm defect group with uncompromised healing. In
232 the collagen+BMP-2 group bone formation mainly took place in the periosteal regions and
233 the defect periphery, whereas in the 0.9mm defect group bone formation mainly took place
234 in the defect center. The collagen group showed similar values compared to the 2.0mm
235 defect group indicating impaired healing, suggesting that the collagen scaffold might have
236 blocked endosteal callus formation.
237 In the FC VOI, we saw a similar pattern in all indices for the collagen and the collagen+BMP-2
238 group without any significant differences between groups. Specifically, the bone formation
239 rate did not significantly change over time in both groups. Similar to the 2mm defect group
240 from Experiment 1, a significant induction of bone resorption rate was seen from week 0-1
241 to week 1-2. From week 1 until the study end, the bone volume significantly ($p<0.0001$)

242 decreased in both groups (collagen group: -48%, collagen+BMP-2 group: -44%).
243 Furthermore, a significant decline in the fraction of highly mineralized bone was observed in
244 both groups from week 0 to week 6 (collagen group: -9%, p=0.0002; collagen+BMP-2 group:
245 -13%, p<0.0001), as similarly observed for the 2mm defect group in Experiment 1 (-16%,
246 p=0.003).
247
248 Cortical bridging occurred by week 2 in 100% of the animals in the collagen+BMP-2 group,
249 whereas no animal in the collagen group showed bridged cortices at this time point (Table
250 2). In the BMP-2 treated defects, cortical bridging also occurred 1 week earlier compared to
251 the 0.9mm defect group from Experiment 1. In contrast, in the collagen group only 1 animal
252 showed cortical bridging and 87.5% manifested as non-unions.
253
254 **Histology**
255 As shown by Safranin-O staining six weeks after osteotomy, hardly any cartilage residuals
256 were present in the defect region in all groups, indicating progression of the healing process
257 to the final remodelling stage (Fig. 5, Row 1 and 2). To visualize potential remnants of the
258 collagen scaffolds in Experiment 2, 1-2 samples/group were stained with Sirius-Red (Fig. 5,
259 Row 3 and 4). For comparisons, we also included sections of the original collagen scaffolds
260 (Fig. 5, Row 5), where red color of the filaments is indicative of collagen. In contrast, no red
261 signal indicative of collagen was seen in the defect center of both groups (Fig. 5, Row 4). This
262 suggested complete degradation of the scaffolds with accumulation of fat cells in the defect
263 (unbridged defects in collagen group and in the restored medullary cavity, bridged defects in
264 the collagen+BMP-2 group; Fig. 5, Row 4).

Discussion

In this study, we showed that time-lapsed *in vivo* micro-CT allows for spatio-temporal discrimination between physiological and impaired fracture healing patterns in a mouse femur defect model. For this purpose, we compared the healing pattern in three callus sub-volumes and the adjacent cortical fragments in a small (0.9mm) and a large (2.0mm) defect group using a previously developed two-threshold density micro-CT protocol [21,22]. In a second step, we applied the micro-CT based monitoring approach for the characterization of the bone regeneration capacity of biomaterials using porous collagen scaffolds +/- bone morphogenetic protein (BMP-2) as test materials.

By registering consecutive scans, we were able to include dynamic parameters such as bone formation and resorption in our micro-CT based monitoring approach as previously described [21]. In the small defect group (0.9mm), this allowed for characterization of the different healing phases seen by changes in formation and resorption in the osseous callus volume. Specifically, we saw that the initiation of bone formation (maximum in week 1-2), indicating the onset of the reparative phase, triggered bone resorption (maximum in week 2-3) thereby initiating the remodelling phase. Maximum osseous callus volumes were observed in week 3, which remained stable until the study end, while the callus mineralization increased throughout the healing period. The observed bone turnover (bone formation triggering bone resorption) and callus maturation (increasing mineralization of initial callus) patterns are similar to a recent study in 1.5mm defects, which showed an uncompromised healing pattern [22]. However, the smaller defect size (- 40%) in the current study, changed the temporal occurrence of peaks in bone formation and resorption, which

288 were seen one week earlier compared to the previous study in 1.5mm defects, indicating
289 faster healing progression.
290 As expected from literature [23], the larger defects (2.0mm) showed impaired healing
291 predominantly leading to non-unions in 7 of 8 animals at the study end (Fig. 2, Table 1). This
292 is in line with a study by Zwingenberger at al. [23], which previously showed a strong
293 correlation of the defect size and non-unions assessed via *in vivo* x-ray measurements as
294 well as end point micro-CT and histological analyses in a similar defect model. Via
295 registration of consecutive *in vivo* micro-CT scans, we were now able to reveal and visualize
296 the preceding spatio-temporal deviations in callus formation and remodelling compared to
297 the uncompromised healing pattern seen in the 0.9mm defect group. Deviations from
298 normal healing occurred in all callus sub-volumes (defect center, defect periphery, cortical
299 fragment periphery), although initiation of bone formation was not changed spatio-
300 temporally, starting in the same sub-volumes (DC, FP) and at the same time (week 0-1 to
301 week 1-2). However, the rise in bone formation was significantly lower endosteally and the
302 duration of the bone formation was reduced periosteally compared to the 0.9mm defect
303 group. This also led to only small endosteal and peripheral callus dimensions with the
304 periosteal callus volume even decreasing to baseline values by the study end. Under normal
305 healing conditions, callus formation in this femur defect model proceeds from both the
306 endosteal and the periosteal regions to the defect periphery [22,24], whereas in large defects
307 hardly any bone formation was seen here, suggesting early termination of the fracture
308 healing process.
309 It is important to separately look at the adjacent cortical fragments [22], where we previously
310 saw an opposite trend in bone turnover compared to the callus sub-volumes. Whereas bone

311 formation was the dominant factor in the callus VOIs, bone resorption was the main factor in
312 the adjacent cortex. In the current study, increased defect size was associated with a
313 significant higher decline in cortical bone volume (-67% vs. -19%) and bone mineral density (-
314 16% vs. -6%; Fig. 1 and Fig. 2). Peri-fracture bone resorption and demineralization of cortical
315 bone have also been previously reported in preclinical and clinical studies and were
316 associated with stiff fixation leading to stress shielding of the bone [25,26]. Our recently
317 developed time-lapsed *in vivo* micro-CT monitoring approach therefore allowed to precisely
318 characterize the spatio-temporal changes in structural and dynamic callus parameters
319 preceding non-unions.
320 In a next step, we applied this monitoring approach to evaluate the bone regeneration
321 potential of biomaterials using collagen +/- BMP-2 as test materials. We selected collagen as
322 test material due to its wide usage in scaffolds intended for promotion of bone regeneration
323 and the comprehensive literature on its performance in *in vitro*, preclinical and clinical
324 applications [27-29]. In our study, the application of collagen scaffolds did not significantly
325 improve bone regeneration compared to empty defects of the same size, with the same
326 non-union rates being observed at the study end (87.5% in both groups). Although periosteal
327 bone formation was more pronounced in the collagen group, the fracture healing outcome
328 was not different between groups. This is in line with previous bone defect studies in
329 different rodent models (loaded and non-loaded bones) reporting no significant effect of
330 collagen scaffolds on bone regeneration with incomplete bone union or non-unions at the
331 study end [30,31]. Similarly, in large animal models collagen scaffolds either failed to prevent
332 non-unions [32] or to restore the mechanical bone properties [33]. The low regeneration
333 potential of collagen scaffolds has been attributed to a general lack of bioactivity of collagen

despite its overall favorable features such as low antigenicity, high biodegradability and high biocompatibility [27-29]. Furthermore, studies indicate a high relevance of the pore size in the collagen scaffolds, with smaller pores potentially being affected by cellular occlusion, and preventing cellular penetration, production of extracellular matrix and neovascularization of the inner areas of the scaffold [28]. In contrast, larger pores have been associated with low mechanical scaffold properties and early scaffold degradation [34,35]. A major limitation of most studies is that they did not include empty defect and positive controls, which would be essential for better understanding of specific changes in healing patterns mediated by different biomaterials.

To further promote bone healing, scaffolds have been incubated in solutions containing growth factors (e.g. BMP-2, BMP-7; [36,37]). Especially BMP-2 has been widely applied in preclinical studies to promote healing of critical sized defects (for review see [38]) and in clinical settings. However, studies reported BMP-2 associated adverse events and complications (e.g. antibody formation, inflammation, ectopic bone formation, carcinogenicity [39-41]). Therefore, using low BMP-2 dosages seems crucial in order to avoid adverse effects while preserving its osteoanabolic potential [42]. So far preclinical studies used a wide range of BMP-2 dosages (0.1-150.000 µg BMP-2 per defect in small animals as summarized in a comprehensive review by Gothard et al. [38]). In this study, we therefore down-scaled the BMP-2 dosages from previous studies (low BMP-2 dosages with beneficial effect on bone healing; 10/75 µg BMP-2 per defect [43,44]) to the volume of our scaffold (2 µg BMP-2 per defect). Similar to other studies [38], BMP-2 application significantly accelerated the healing process leading to early cortical bridging. However, when looking at the defect sub-volumes separately, we saw that the spatio-temporal healing pattern largely differed from the physiological healing pattern seen in the 0.9mm group. In the collagen+BMP-2

358 group the increase in the bone formation rate was higher but persisted for a shorter amount
359 of time compared to the 0.9mm defect group. Furthermore, bone formation mainly took
360 place in the periosteal regions and the defect periphery, whereas in the 0.9mm defect group
361 bone formation was predominantly seen in the defect center. This supports the assumption
362 that the collagen scaffold itself might have hindered cells from migrating into the defect
363 center. In line with other studies [30,45], the collagen scaffolds were degraded in both groups
364 by the end of the study as shown by absence of collagen fibers in the defect center via Sirius
365 Red staining of histological sections. Accumulation of fat cells inside the formed cortical shell
366 (unions) or in the defect center (non-unions) indicated differentiation of mesenchymal stem
367 cells (MSCs) towards the adipogenic lineage in the later healing period. Concluding from the
368 time-lapsed *in vivo* micro-CT evaluation, strong BMP-2 induced bone formation associated
369 with osteogenic differentiation of MSCs was only transiently observed in the early healing
370 period. Removal of the BMP-2 induced stimulus in later healing phases might have caused a
371 change from osteogenic to adipogenic differentaion of MSCs. This shift might have been
372 further strengthened by stress shielding of the defect region associated with stiff external
373 fixation [46].
374 Our study therefore shows that sub-volume specific characterization of biomaterials seems
375 crucial for assessing their bone regeneration potential. The study further indicates that time-
376 lapsed *in vivo* micro-CT combined with our recently developed two-threshold density
377 approach should be used in future studies to identify parameters for prediction of non-
378 unions in early healing phases. Via registration of consecutive scans as described recently,
379 we were able to precisely characterize and understand which spatio-temporal deviations led
380 to non-union formation and how this was prevented by BMP-2 application. Using collagen

381 and BMP-2 as test materials, the time-lapsed *in vivo* micro-CT-based monitoring approach
382 was shown to be suitable for spatio-temporal assessment of callus formation and
383 remodelling patterns and could be used in future studies to characterize and precisely
384 understand the regeneration capacity of novel biomaterials.

385 The current study has several limitations. We did not track the degradation of the collagen
386 scaffolds over time and only performed end-point histological assessment of collagen
387 residuals via Sirius Red staining. Future studies should apply fluorescent biomaterials and
388 reporters, which could be visualized via *in vivo* optical imaging [47-49]. We did also not measure
389 the BMP-2 release kinetics. This could be similarly achieved via the use of fluorescently-
390 labeled growth factors[50] in combination with multimodal imaging (e.g. photoacoustic
391 imaging, PET, SPECT, micro-CT)[17,51]. Furthermore, in order to reliably create critical-sized
392 defects, the defect size would need to be increased by ca. 25% in future studies.

393 Nevertheless, application of time-lapsed *in vivo* micro-CT allows faster and more precise
394 evaluation of biomaterials for bone regeneration, thereby also reducing the animal numbers
395 involved according to the 3R's of animal welfare. It could further be used for early prediction
396 of non-union formation and identification of biomarkers. The approach could be
397 supplemented with the registration of 2D-histology section into the 3D-micro-CT volume[52],
398 potentially allowing for a spatio-temporal understanding of molecular and cellular changes
399 induced by different biomaterials. To better mimic the clinical situation, future studies
400 should also assess the performance of biomaterials under load application, which could be
401 achieved using a recently developed loading fixator[53]. By combining our *in vivo* time-lapsed
402 micro-CT based monitoring approach with individualized loading regimes, this would allow
403 for thorough characterization of biomaterials under clinically relevant loading conditions.

404 To conclude, *in vivo* time-lapsed micro-CT allows (1) spatio-temporal discrimination between
405 normal and disturbed healing patterns relevant for the detection of distinct features
406 associated with different medical conditions and (2) spatio-temporal characterization of the
407 bone regeneration capacity of biomaterials.
408

409 **Materials and Methods**

410 **Animals**

411 All animal procedures were approved by the local authorities (licence number: 36/2014;
412 Kantonales Veterinäramt Zürich, Zurich, Switzerland). We confirm that all methods were
413 carried out in accordance with relevant guidelines and regulations (Swiss Animal Welfare Act
414 and Ordinance (TSchG, TSchV)) and reported considering ARRIVE guidelines. Female 12
415 week-old C57BL/6J mice were purchased from Janvier (Saint Berthevin Cedex, France) and
416 housed in the animal facility of the ETH Phenomics Center (EPIC; 12h:12h light-dark cycle,
417 maintenance feed (3437, KLIBA NAFAG, Kaiseraugst, Switzerland), 5 animals/cage). At an age
418 of 20 weeks, all animals received a femur defect. In Experiment 1, one group of animals
419 received a small defect (defect length: 0.86±0.09mm, n=10) and a second group received a
420 large defect (defect length: 2.00±0.19mm, n=8; housing after surgery: 2-3 animals/cage). In
421 Experiment 2 both groups received a 2mm femur defect with application of either collagen
422 scaffolds (d=2mm, h=2mm; ILS, Saint Priest, France; n=8) or collagen scaffolds+BMP-2
423 (2.5µg/scaffold; PeproTech, London, UK; n=8). Perioperative analgesia (25 mg/L, Tramal®,
424 Gruenenthal GmbH, Aachen, Germany) was provided via the drinking water two days before
425 surgery until the third postoperative day. For surgery and micro-CT scans, animals were
426 anesthetized with isoflurane (induction/maintenance: 5%/1-2% isoflurane/oxygen).

427

428 **Femur defect**

429 An external fixator (Mouse ExFix, RISystem, Davos, Switzerland; stiffness: 24N/mm[21]) was
430 positioned at the craniolateral aspect of the right femur and attached using four mounting
431 pins. First, the most distal pin was inserted approximately 2mm proximal to the growth
432 plate, followed by placement of the most proximal and the inner pins. Subsequently, a femur
433 defect was created using 1 and 2 Gigli wire saws for the small and the large defect,
434 respectively.

435

436 **Time-lapsed *in vivo* micro-CT**

437 Immediate post-surgery correct positioning of the fixator and the defect was visualized using
438 a vivaCT 40 (Scanco Medical AG, Brüttisellen, Switzerland) (isotropic nominal resolution: 10.5
439 µm; 55 kVp, 145 µA, 350 ms integration time, 500 projections per 180°, 21 mm field of view
440 (FOV), scan duration ca. 15 min). Subsequently, the defect region as well as the adjacent
441 cortex were scanned weekly (week 1-6) with the same settings and morphometric indices
442 and mineralization progression were determined in four volumes of interest (for details on
443 methods see [21,22]): defect center (DC), defect periphery (DP), cortical fragment center (FC),
444 and fragment periphery (FP). Data were normalised to the central VOIs: DC/DC, DP/DC,
445 FC/FC, FP/FC. Cortical bridging was assessed as previously described in [22].

446

447 **Animations**

448 To further visualize the defect healing process and the VOIs involved, 3-dimensional
449 computer renderings were created from the time-lapsed micro-CT data for one mouse in

450 each respective group across both experiments (0.9mm defect group, 2.0mm defect group,
451 collagen scaffold, collagen scaffold+BMP-2), then animated and captioned to create videos
452 (Supplementary Video 1, Supplementary Video 2). Bone mineral density data was single-
453 value thresholded (BMD = 395 mg HA/cm^3) at each time point to create a binary array,
454 simplifying the rendering process. This binarized bone location data was interpolated using a
455 Euclidean Distance Transform, generating data for time points in between each weekly
456 measurement. This data was used to create smooth, animated transitions from one
457 measurement to the next, for visualization purposes, and was not used in any analysis. To
458 indicate bone formation and resorption between each time point, bone remodelling data
459 from the time-lapsed *in vivo* micro-CT method was taken [21]. Depictions of the VOIs were
460 rendered directly from their location data used in this approach. All renderings of the 3D
461 data were performed in Paraview (Kitware, Version 5.6). All numerical analysis used for the
462 animations was done using custom Python 3 scripts. Video editing and captioning was done
463 in Hitfilm Express (FXhome, Version 13).
464

465 **Histology**

466 To exemplarily visualize the defect region, histology was performed in 1-2 animals/group. On
467 day 42 femurs were excised, the femoral head was removed, and the samples were placed in
468 4% neutrally buffered formalin for 24 hours and subsequently decalcified in 12.5% EDTA for
469 10-14 days. The samples were embedded in paraffin and 4.5 µm longitudinal sections were
470 stained with Safranin-O/Fast Green: Weigert's iron haematoxylin solution (HT1079, Sigma-
471 Aldrich, St. Louis, MO) - 4min, 1:10 HCl-acidified 70% ethanol – 10s, tap water - 5min, 0.02%
472 Fast Green (F7258, Sigma-Aldrich, St. Louis, MO) - 3min, 1% acetic acid - 10s, 0.1% Safranin-

473 O (84120, Fluka, St. Louis, MO) - 5min. In order to visualize remnants of the collagen
474 scaffolds, Sirius Red staining was performed in 1 animal from the collagen and 1 animal from
475 the collagen+BMP-2 group. For comparison, we also stained sections of the original collagen
476 matrix with Sirius-Red: Weigert's iron haematoxylin solution (HT1079, Sigma-Aldrich, St.
477 Louis, MO) - 8min, tap water - 10min, 1:9 Picro-Sirius Red solution (Picric acid: 80456, Fluka,
478 St. Louis, MO; Direct Red 80: AB133584, ABCR, Karlsruhe, Germany) - 1h, 5% acetic acid
479 2x10s. For both stainings, images were taken with Slide Scanner Pannoramic 250 (3D
480 Histech, Budapest, Hungary) at 20x magnification.
481
482 **Statistics**
483 CT analysis: Data were tested for normal distribution (Shapiro-Wilk-Test) and homogeneity
484 of variance (Levene-Test). Depending on the test outcome, group comparisons of data
485 derived at single time points were done by Student's t-test or Mann-Whitney U-tests (IBM
486 SPSS Statistics Version 23). For statistical evaluation of repeated measurements two-way
487 ANOVA with Geisser-Greenhouse correction and Bonferroni correction (GraphPad Prism 8)
488 were performed. The level of significance was set at $p < 0.05$.
489
490 **Author Contributions Statement**
491 The study was designed by E.W., G.A.K., S.H. and R.M.. The *in vivo* experiments were
492 performed by E.W., G.A.K. and E.F.. Histological stainings were performed by E.W. and
493 M.H.N.. Data analyses were performed by E.W. and D.C.T.B.. Illustrations of VOIs and
494 animations on callus formation and remodelling were made by B.J.S.. The manuscript was
495 written by E.W. and reviewed and approved by all authors.

Data availability

All necessary data generated or analyzed during the present study are included in this published article and its Supplementary Information files (preprint available on BioRxiv (BIORXIV/2020/). Additional information related to this paper may be requested from the authors.

Competing Interests

The authors declare no competing interests.

Acknowledgements

The authors gratefully acknowledge support from the EU (BIODESIGN FP7-NMP-2012-262948 and ERC Advanced MechAGE ERC-2016-ADG-741883). E. Wehrle received funding from the ETH Postdoctoral Fellowship Program (MSCA-COFUND, FEL-25_15-1).

References

1 Giannoudis, P., Tzioupis, C., Almalki, T. & Buckley, R. Fracture healing in osteoporotic fractures: is it really different? A basic science perspective. *Injury* **38 Suppl 1**, S90-99, doi:10.1016/j.injury.2007.02.014 (2007).

2 Syed, A. A., Agarwal, M., Giannoudis, P. V., Matthews, S. J. E. & Smith, R. M. Distal femoral fractures: long-term outcome following stabilisation with the LISS. *Injury-International Journal of the Care of the Injured* **35**, 599-607, doi:10.1016/S0020-1383(03)00247-X (2004).

3 Winkler, T., Sass, F. A., Duda, G. N. & Schmidt-Bleek, K. A review of biomaterials in bone defect healing, remaining shortcomings and future opportunities for bone tissue engineering THE UNSOLVED CHALLENGE. *Bone Joint Res* **7**, 232-243, doi:10.1302/2046-3758.73.Bjr-2017-0270.R1 (2018).

4 Przekora, A. The summary of the most important cell-biomaterial interactions that need to be considered during in vitro biocompatibility testing of bone scaffolds for tissue engineering applications. *Mat Sci Eng C-Mater* **97**, 1036-1051, doi:10.1016/j.msec.2019.01.061 (2019).

5 Stevens, M. M. Biomaterials for bone tissue engineering. *Mater Today* **11**, 18-25, doi:Doi 10.1016/S1369-7021(08)70086-5 (2008).

6 Hulsart-Billstrom, G. *et al.* A Surprisingly Poor Correlation between in Vitro and in Vivo Testing of Biomaterials for Bone Regeneration: Results of a Multicentre Analysis. *Eur Cells Mater* **31**, 312-322, doi:10.22203/eCM.v031a20 (2016).

7 Pearce, A. I., Richards, R. G., Milz, S., Schneider, E. & Pearce, S. G. Animal models for implant biomaterial research in bone: A review. *Eur Cells Mater* **13**, 1-10 (2007).

8 Peric, M. *et al.* The rational use of animal models in the evaluation of novel bone regenerative therapies. *Bone* **70**, 73-86, doi:10.1016/j.bone.2014.07.010 (2015).

9 Gomes, P. S. & Fernandes, M. H. Rodent models in bone-related research: the relevance of calvarial defects in the assessment of bone regeneration strategies. *Lab Anim-Uk* **45**, 14-24, doi:10.1258/la.2010.010085 (2011).

10 Harris, J. S., Bemenderfer, T. B., Wessel, A. R. & Kacena, M. A. A review of mouse critical size defect models in weight bearing bones. *Bone* **55**, 241-247, doi:10.1016/j.bone.2013.02.002 (2013).

11 Holstein, J. H. *et al.* Mouse Models for the Study of Fracture Healing and Bone Regeneration. *Osteoporosis Research: Animal Models*, 175-191, doi:10.1007/978-0-85729-293-3_14 (2011).

12 Horner, E. A. *et al.* Long Bone Defect Models for Tissue Engineering Applications: Criteria for Choice. *Tissue Eng Part B-Re* **16**, 263-271, doi:10.1089/ten.teb.2009.0224 (2010).

13 van Griensven, M. Preclinical testing of drug delivery systems to bone. *Adv Drug Deliver Rev* **94**, 151-164, doi:10.1016/j.addr.2015.07.006 (2015).

14 Gauthier, O. *et al.* In vivo bone regeneration with injectable calcium phosphate biomaterial: A three-dimensional micro-computed tomographic, biomechanical and SEM study. *Biomaterials* **26**, 5444-5453, doi:10.1016/j.biomaterials.2005.01.072 (2005).

15 Martino, M. *et al.* Growth factors engineered for super-affinity to extracellular matrix enhance tissue healing. *J Tissue Eng Regen M* **8**, 35-36 (2014).

16 Meinel, L. *et al.* Silk based biomaterials to heal critical sized femur defects. *Bone* **39**, 922-931, doi:10.1016/j.bone.2006.04.019 (2006).

17 Lienemann, P. S. *et al.* Longitudinal in vivo evaluation of bone regeneration by combined measurement of multi-pinhole SPECT and micro-CT for tissue engineering (vol 5, 10238, 2015). *Sci Rep-Uk* **5**, doi:ARTN 1239110.1038/srep12391 (2015).

18 van Lenthe, G. H. *et al.* Nondestructive micro-computed tomography for biological imaging and quantification of scaffold-bone interaction in vivo. *Biomaterials* **28**, 2479-2490, doi:10.1016/j.biomaterials.2007.01.017 (2007).

19 Boerckel, J. D. *et al.* Effects of protein dose and delivery system on BMP-mediated bone regeneration. *Biomaterials* **32**, 5241-5251, doi:10.1016/j.biomaterials.2011.03.063 (2011).

20 Mehta, M., Checa, S., Lienau, J., Hutmacher, D. & Duda, G. N. In Vivo Tracking of Segmental Bone Defect Healing Reveals That Callus Patterning Is Related to Early Mechanical Stimuli. *Eur Cells Mater* **24**, 358-371, doi:DOI 10.22203/eCM.v024a26 (2012).

21 Tourolle né Betts, D. W., E.; Paul, GR; Kuhn, GA; Christen, P; Hofmann, S; Müller, R. The association between mineralised tissue formation and the mechanical local in vivo environment: Time-lapsed quantification of a mouse defect healing model. *Sci Rep-Uk* **10**, 1100, doi:doi: https://doi.org/10.1038/s41598-020-57461-5 (2020).

22 Wehrle E, T. n. B. D., Kuhn GA, Scheuren AC, Hofmann S, Müller R. Evaluation of longitudinal time-lapsed in vivo micro-CT for monitoring fracture healing in mouse femur defect models. *Sci Rep-Uk* **9**, 17445, doi:doi: https://doi.org/10.1038/s41598-019-53822-x (2019).

23 Zwingenberger, S. *et al.* Establishment of a femoral critical-size bone defect model in immunodeficient mice. *J Surg Res* **181**, E7-E14, doi:10.1016/j.jss.2012.06.039 (2013).

24 Borgiani, E. *et al.* Age-Related Changes in the Mechanical Regulation of Bone Healing Are Explained by Altered Cellular Mechanoresponse. *J Bone Miner Res*, doi:10.1002/jbmr.3801 (2019).

25 Al-Tamimi, A. A., Peach, C., Fernandes, P. R., Cseke, A. & Bartolo, P. J. D. S. Topology Optimization to reduce the stress shielding effect for orthopedic applications. *Proc Cirp* **65**, 202-206, doi:10.1016/j.procir.2017.04.032 (2017).

26 Bobyn, J. D. *et al.* The effect of stem stiffness on femoral bone resorption after canine porous-coated total hip arthroplasty. *Clin Orthop Relat Res*, 196-213 (1990).

27 Zhang, D. W., Wu, X. W., Chen, J. D. & Lin, K. L. The development of collagen based composite scaffolds for bone regeneration. *Bioact Mater* **3**, 129-138, doi:10.1016/j.bioactmat.2017.08.004 (2018).

28 Ferreira, A. M., Gentile, P., Chiono, V. & Ciardelli, G. Collagen for bone tissue regeneration. *Acta Biomater* **8**, 3191-3200, doi:10.1016/j.actbio.2012.06.014 (2012).

29 Glowacki, J. & Mizuno, S. Collagen scaffolds for tissue engineering. *Biopolymers* **89**, 338-344, doi:10.1002/bip.20871 (2008).

30 Hertweck, J. *et al.* CD34(+) cells seeded in collagen scaffolds promote bone formation in a mouse calvarial defect model. *J Biomed Mater Res B Appl Biomater* **106**, 1505-1516, doi:10.1002/jbm.b.33956 (2018).

31 Stuckensen, K. *et al.* Anisotropic Cryostructured Collagen Scaffolds for Efficient Delivery of RhBMP-2 and Enhanced Bone Regeneration. *Materials (Basel)* **12**, doi:10.3390/ma12193105 (2019).

32 Cipitria, A. *et al.* BMP delivery complements the guiding effect of scaffold architecture without altering bone microstructure in critical-sized long bone defects: A multiscale analysis. *Acta Biomater* **23**, 282-294, doi:10.1016/j.actbio.2015.05.015 (2015).

33 Sarkar, M. R. *et al.* Bone formation in a long bone defect model using a platelet-rich plasma-loaded collagen scaffold. *Biomaterials* **27**, 1817-1823, doi:10.1016/j.biomaterials.2005.10.039 (2006).

34 Karageorgiou, V. & Kaplan, D. Porosity of 3D biomaterial scaffolds and osteogenesis. *Biomaterials* **26**, 5474-5491, doi:10.1016/j.biomaterials.2005.02.002 (2005).

35 Luo, Z. W. *et al.* Effect of Pore Size on the Biodegradation Rate of Silk Fibroin Scaffolds. *Adv Mater Sci Eng*, doi:Artn 31539710.1155/2015/315397 (2015).

36 Begam, H., Nandi, S. K., Kundu, B. & Chanda, A. Strategies for delivering bone morphogenetic protein for bone healing. *Mat Sci Eng C-Mater* **70**, 856-869, doi:10.1016/j.msec.2016.09.074 (2017).

37 Salazar, V. S., Gamer, L. W. & Rosen, V. BMP signalling in skeletal development, disease and repair. *Nat Rev Endocrinol* **12**, 203-221, doi:10.1038/nrendo.2016.12 (2016).

38 Gothard, D. *et al.* Tissue Engineered Bone Using Select Growth Factors: A Comprehensive Review of Animal Studies and Clinical Translation Studies in Man. *Eur Cells Mater* **28**, 166-208, doi:DOI 10.22203/eCM.v028a13 (2014).

39 James, A. W. *et al.* A Review of the Clinical Side Effects of Bone Morphogenetic Protein-2. *Tissue Eng Part B-Re* **22**, 284-297, doi:10.1089/ten.teb.2015.0357 (2016).

40 Skovrlj, B. *et al.* Association Between BMP-2 and Carcinogenicity. *Spine* **40**, 1862-1871, doi:10.1097/Brs.0000000000001126 (2015).

41 Tannoury, C. A. & An, H. S. Complications with the use of bone morphogenetic protein 2 (BMP-2) in spine surgery. *Spine J* **14**, 552-559, doi:10.1016/j.spinee.2013.08.060 (2014).

618 42 Schmidt-Bleek, K., Willie, B. M., Schwabe, P., Seemann, P. & Duda, G. N. BMPs in bone
619 regeneration: Less is more effective, a paradigm-shift. *Cytokine Growth F R* **27**, 141-148,
620 doi:10.1016/j.cytogfr.2015.11.006 (2016).
621 43 Karageorgiou, V. *et al.* Porous silk fibroin 3-D scaffolds for delivery of bone morphogenetic
622 protein-2 in vitro and in vivo. *J Biomed Mater Res A* **78**, 324-334, doi:10.1002/jbm.a.30728
623 (2006).
624 44 Zhang, W. *et al.* VEGF and BMP-2 promote bone regeneration by facilitating bone marrow
625 stem cell homing and differentiation. *Eur Cell Mater* **27**, 1-11; discussion 11-12,
626 doi:10.22203/ecm.v027a01 (2014).
627 45 Hollinger, J. O. *et al.* Recombinant human bone morphogenetic protein-2 and collagen for
628 bone regeneration. *J Biomed Mater Res* **43**, 356-364, doi:10.1002/(sici)1097-
629 4636(199824)43:4<356::aid-jbm3>3.0.co;2-7 (1998).
630 46 Herberg, S. *et al.* Combinatorial morphogenetic and mechanical cues to mimic bone
631 development for defect repair. *Sci Adv* **5**, doi:ARTN eaax247610.1126/sciadv.aax2476 (2019).
632 47 Fragogeorgi, E. A. *et al.* In vivo imaging techniques for bone tissue engineering. *J Tissue Eng*
633 **10**, doi:Artn 204173141985458610.1177/2041731419854586 (2019).
634 48 Gil, C. J. *et al.* In Vivo Tracking of Tissue Engineered Constructs. *Micromachines-Basel* **10**,
635 doi:ARTN 47410.3390/mi10070474 (2019).
636 49 Li, K. & Liu, B. Polymer-encapsulated organic nanoparticles for fluorescence and
637 photoacoustic imaging. *Chem Soc Rev* **43**, 6570-6597, doi:10.1039/c4cs00014e (2014).
638 50 Mafina, M. K., Sullivan, A. C. & Hing, K. A. Use of a fluorescent probe to monitor the
639 enhanced affinity of rh-BMP-2 to silicated-calcium phosphate synthetic bone graft
640 substitutes under competitive conditions. *Mat Sci Eng C-Mater* **80**, 207-212,
641 doi:10.1016/j.msec.2017.05.142 (2017).
642 51 Hulsart-Billstrom, G. *et al.* Non-invasive tri-modal visualisation via PET/SPECT/mu CT of
643 recombinant human bone morphogenetic protein-2 retention and associated bone
644 regeneration: A proof of concept. *J Control Release* **285**, 178-186,
645 doi:10.1016/j.jconrel.2018.07.012 (2018).
646 52 Taylor, C., Scheuren, A., Trüssel, A. & R., M. 3D local in vivo environment (LivE) imaging for
647 single cell protein analysis of bone tissue. . *Current Directions in Biomedical Engineering* **2**
648 (2016).
649 53 Wehrle E., P. G. R., Betts D.C., Kuhn G.A., Müller R. Individualized cyclic mechanical loading
650 improves callus properties in novel femur fracture loading model as assessed by time-lapsed
651 in vivo imaging and real-time micro-finite element analysis. . *Trans. Orthop. Res. Soc.* **44**,
652 1526 (2019).

653

654 **Figure legends**

655 **Figure 1.** Representative images (threshold: 645 mg HA/cm^3) of the defect region from
656 animals of the 0.9mm group (top) and the 2.0mm group (bottom).
657 Visualization of bone formation (orange) and resorption (blue) via registration of micro-CT
658 scans from weeks 1-6 to weeks 0-5.

659 **Figure 2**. Micro-CT based evaluation of bone parameters in the 0.9mm group (blue) and the
660 2.0mm group (red) using different VOIS: defect center (DC; a-c), defect periphery (DP; d-f),
661 cortical fragment center (FC; g-i), cortical fragment periphery (FP; j-l). a, d, g, j: Bone
662 formation rate (solid line) and bone resorption rate (dashed line) given in percent per day. b,
663 e, h, k: Bone volume (BV) normalized to TV (DC for DC and DP, FC for FC+FP). c, f, i, l: Degree
664 of bone mineralization given as ratio of bone volume with a density ≥645 mg HA/cm^3 to the
665 total osseous volume (threshold ≥395 mg HA/cm^3). n=7/10; a,d,g,j: * indicates $p < 0.05$
666 between consecutive weeks; # indicates $p < 0.05$ between groups. b,c,e,f,h,I,k,l: * indicates p
667 < 0.05 between groups; # indicates $p < 0.05$ between consecutive weeks.

668 **Figure 3.** Representative images (threshold: 645 mg HA/cm^3) of the defect region from
669 animals of the collagen group (top) and the collagen+BMP-2 group (bottom). Visualization of
670 bone formation (orange) and resorption (blue) via registration of micro-CT scans from weeks
671 1-6 to weeks 0-5.

672 **Figure 4.** Micro-CT based evaluation of bone parameters in the collagen group (blue) and the
673 collagen+BMP-2 group (red) using different VOIS: defect center (DC; a-c), defect periphery
674 (DP; d-f), cortical fragment center (FC; g-i), cortical fragment periphery (FP; j-l). a, d, g, j:
675 Bone formation rate (solid line) and bone resorption rate (dashed line) given in percent per
676 day. b, e, h, k: Bone volume (BV) normalized to TV (DC for DC and DP, FC for FC+FP). c, f, i, l:
677 Degree of bone mineralization given as ratio of bone volume with a density ≥645 mg HA/cm^3
678 to the total osseous volume (threshold ≥395 mg HA/cm^3). n=7/10; a,d,g,j: * indicates $p <$
679 0.05 between consecutive weeks; # indicates $p < 0.05$ between groups. b,c,e,f,h,I,k,l: *
680 indicates $p < 0.05$ between groups; # indicates $p < 0.05$ between consecutive weeks.

Figure 5. Histology of longitudinal sections of fractured femora 6 weeks after defect surgery. Row 1: Safranin-O staining of 0.9mm and 2.0mm defect groups - overview images, scale bar = 1 mm and area between inner pins of fixator, scale bar = 100 µm. Row 2: Safranin-O staining of collagen and collagen+BMP-2 groups - overview images, scale bar = 1 mm and area between inner pins of fixator, scale bar = 100 µm. Row 3: Sirius-Red staining of collagen and collagen+BMP-2 groups - overview images, scale bar = 1 mm and area centered between inner pins of fixator, scale bar = 100 µm. Row 4: Sirius-Red staining of defect center of collagen group and collagen+BMP-2 group, scale bar = 50 µm. Row 5: Sirius-Red staining of original collagen matrix, scale bar = 500 µm (left image) and 50 µm (right image).

Tables

Table 1. Number of bridged cortices per callus evaluated weekly in two perpendicular planes and number of mice with successful fracture healing in the 0.9mm and the 2.0mm defect groups (≥ 3 bridged cortices, threshold 395 mg HA/cm^3).

		Number of bridged cortices					Fracture healing outcome	
Week	Group	0	1	2	3	4	Not healed	Healed
0	0.9mm	10	0	0	0	0	10	0
	2.0mm	8	0	0	0	0	8	0
1	0.9mm	10	0	0	0	0	10	0
	2.0mm	8	0	0	0	0	8	0
2	0.9mm	7	3	0	0	0	10	0
	2.0mm	8	0	0	0	0	10	0
3	0.9mm	1	0	2	6	1	3	7
	2.0mm	7	1	0	0	0	8	0
4	0.9mm	1	0	1	5	3	2	8
	2.0mm	7	0	0	1	0	7	1
5	0.9mm	1	0	0	4	5	1	9
	2.0mm	7	0	0	1	0	7	1
6	0.9mm	1	0	0	4	5	1	9
	2.0mm	7	0	0	1	0	7	1

Table 2. Number of bridged cortices per callus evaluated weekly in two perpendicular planes and number of mice with successful fracture healing in the collagen and the collagen+BMP-2 groups (≥ 3 bridged cortices, threshold 395 mg HA/cm^3).

		Number of bridged cortices					Fracture healing outcome	
Week	Group	0	1	2	3	4	Not healed	Healed
0	collagen	8	0	0	0	0	8	0
	collagen+BMP	8	0	0	0	0	8	0
1	collagen	8	0	0	0	0	8	0
	collagen+BMP	8	0	0	0	0	8	0
2	collagen	7	0	1	0	0	8	0
	collagen+BMP	0	0	0	0	8	0	8
3	collagen	7	0	0	1	0	7	1
	collagen+BMP	0	0	0	0	8	0	8
4	collagen	7	0	0	1	0	7	1
	collagen+BMP	0	0	0	0	8	0	8
5	collagen	7	0	0	1	0	7	1
	collagen+BMP	0	0	0	0	8	0	8
6	collagen	7	0	0	1	0	7	1
	collagen+BMP	0	0	0	0	8	0	8

Figure 1

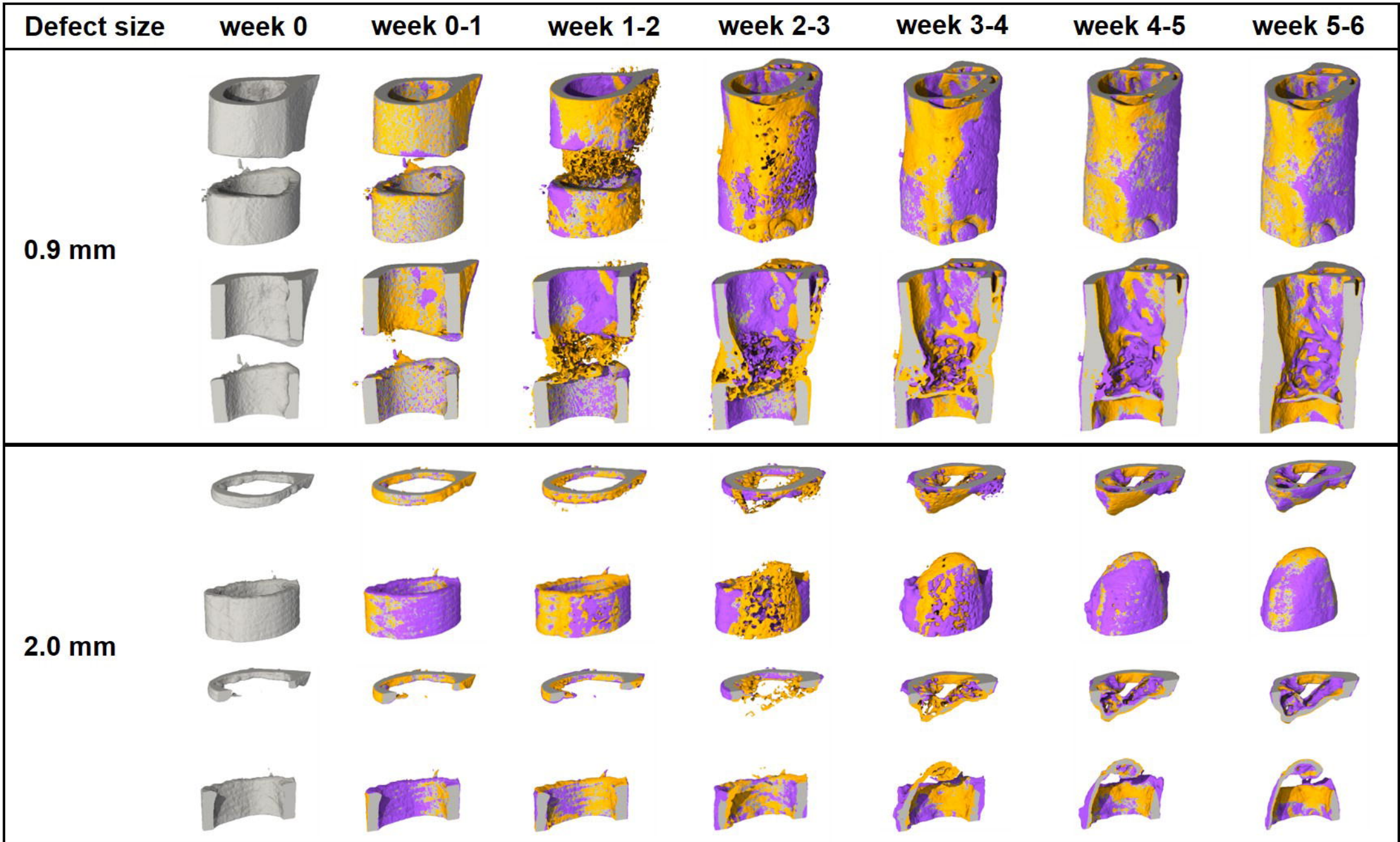
Defect size
week 0
week 0-1
week 1-2
week 2-3
week 3-4
week 4-5
week 5-6
0.9 mm
2.0 mm

Figure 2

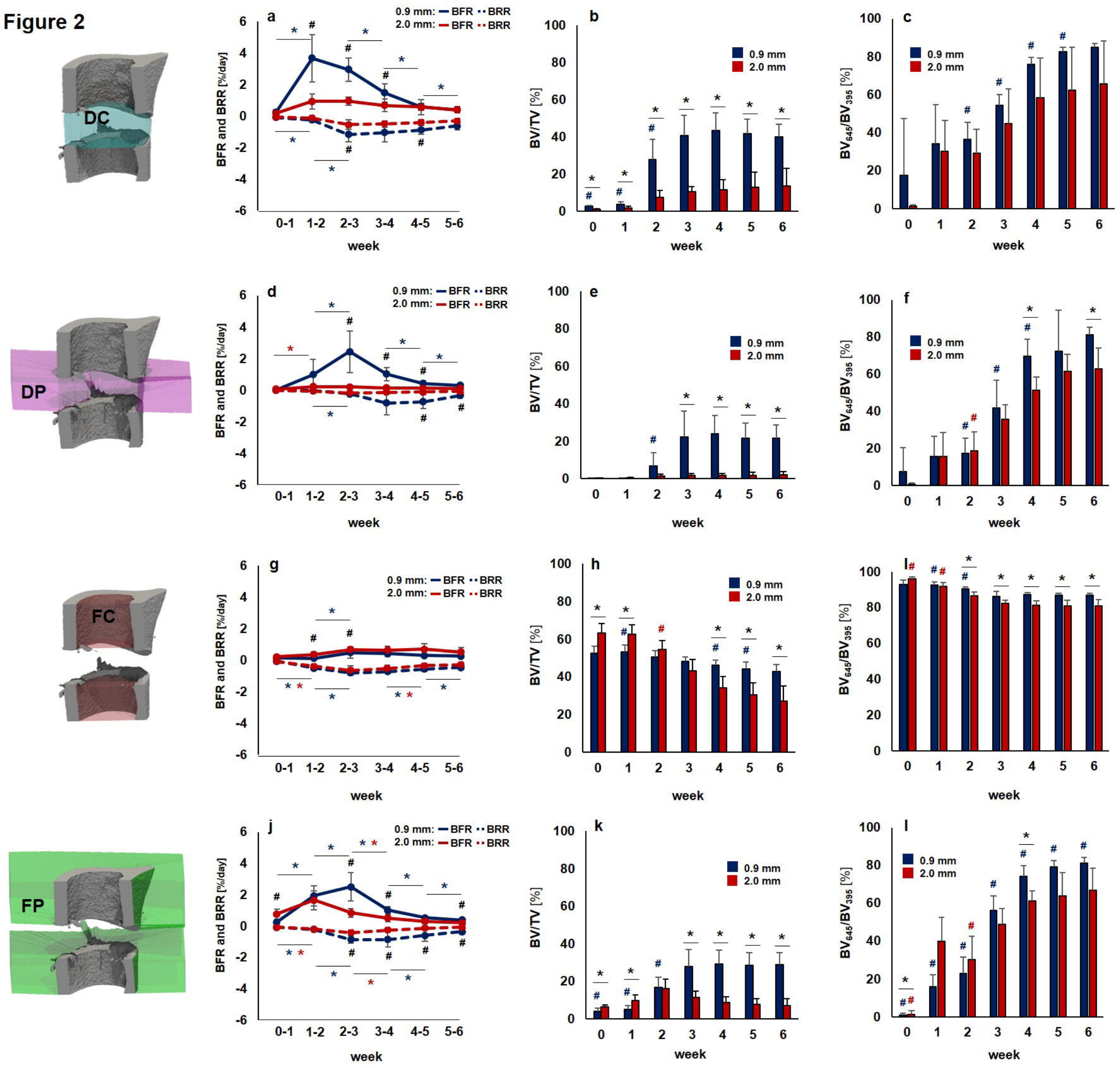
DC
DP
FC
FP
a
b
c
d
e
f
g
h
i
j
k
l
0.9 mm: BFR BRR
2.0 mm: BFR BRR
BFR and BRR [%/day]
BV/TV [%]
BV_{645}/BV_{395} [%]
0.9 mm
2.0 mm
week
0-1
1-2
2-3
3-4
4-5
5-6

Figure 3

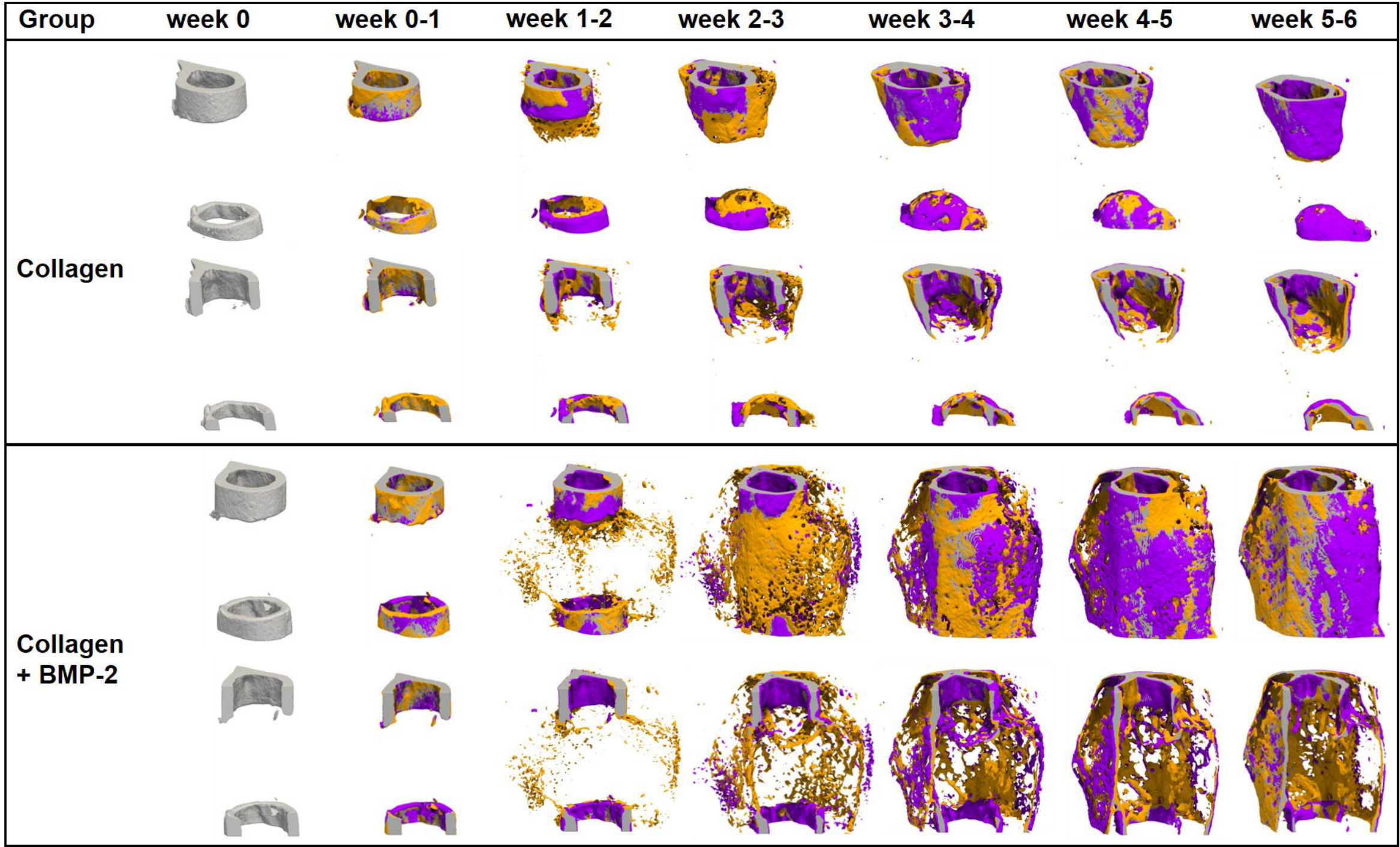
Group
week 0
week 0-1
week 1-2
week 2-3
week 3-4
week 4-5
week 5-6
Collagen
Collagen
+ BMP-2

Figure 4

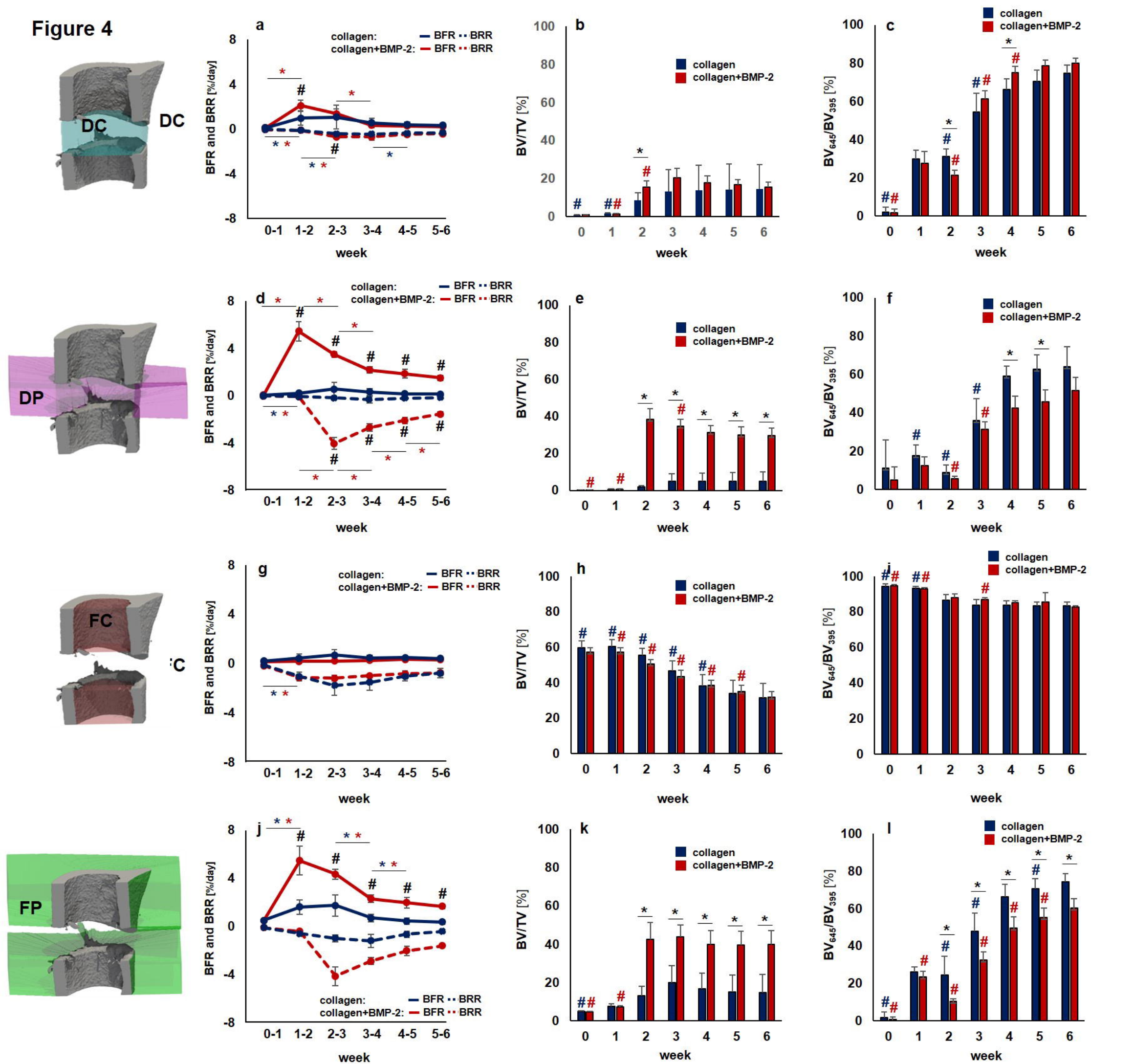
DC
DC
DP
FC
FP
a
b
c
d
e
f
g
h
i
j
k
l
collagen:
collagen+BMP-2:
BFR
BRR
BFR and BRR [%/day]
BV/TV [%]
BV_{645}/BV_{395} [%]
collagen
collagen+BMP-2
week
0-1
1-2
2-3
3-4
4-5
5-6

Figure 5

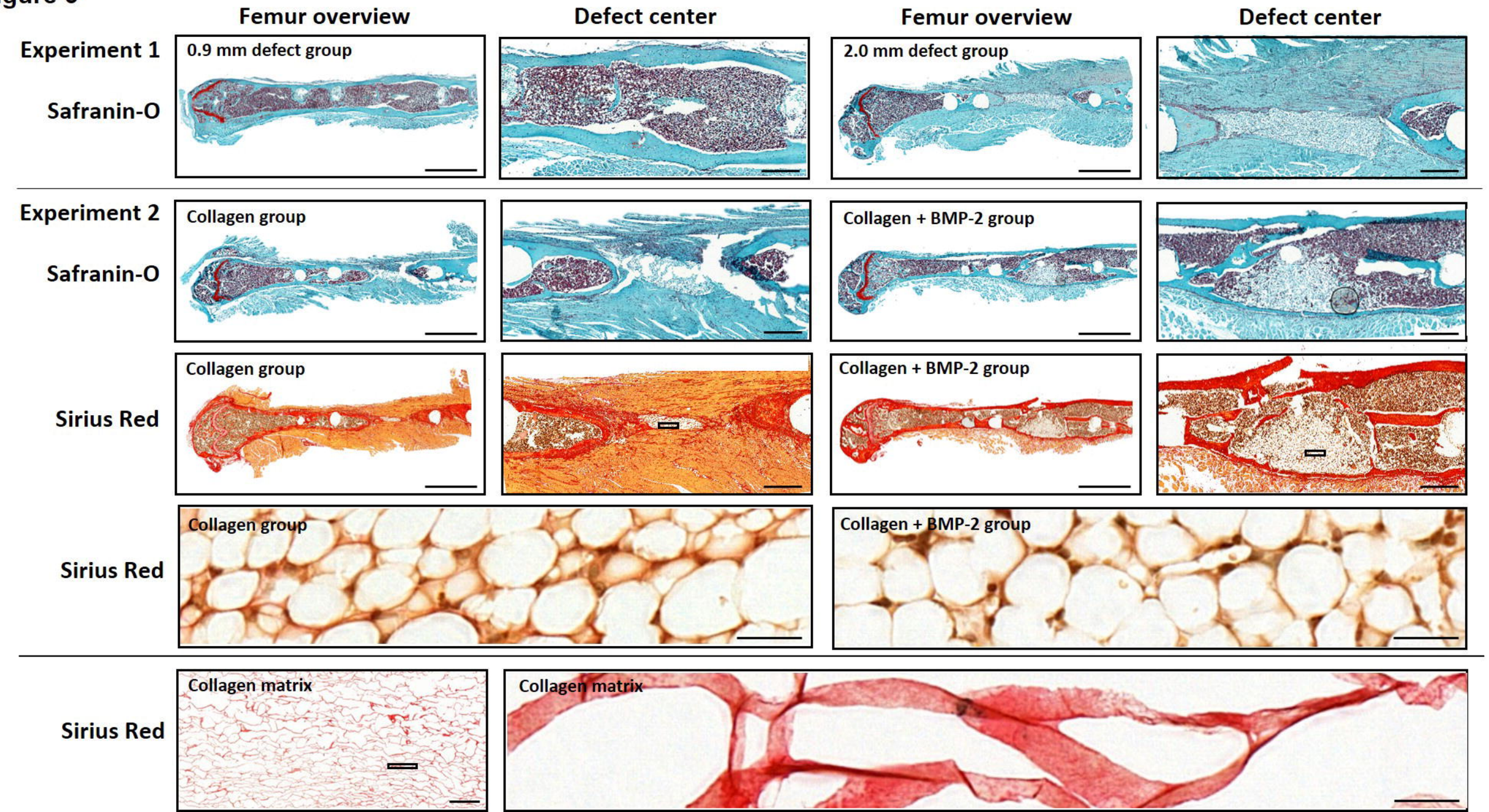
Femur overview
Defect center
Femur overview
Defect center
Experiment 1
Safranin-O
0.9 mm defect group
2.0 mm defect group
Experiment 2
Safranin-O
Collagen group
Collagen + BMP-2 group
Sirius Red
Collagen group
Collagen + BMP-2 group
Sirius Red
Collagen group
Collagen + BMP-2 group
Sirius Red
Collagen matrix
Collagen matrix